



Multiscale label-free imaging of myelin in human brain tissue with polarization-sensitive optical coherence tomography and birefringence microscopy

NATHAN BLANKE,^{1,†,*}  SHUAIBIN CHANG,^{2,†}  ANNA NOVOSELTSEVA,¹ HUI WANG,³ DAVID A. BOAS,¹ AND IRVING J. BIGIO^{1,2}

¹*Department of Biomedical Engineering, Boston University, 44 Cummington Mall, Boston, MA 02215, USA*

²*Department of Electrical & Computer Engineering, Boston University, 8 St. Mary's St., Boston, MA 02215, USA*

³*Department of Radiology, Athinoula A. Martinos Center for Biomedical Imaging, Massachusetts General Hospital, 149 13th St., Charlestown, MA 02129, USA*

[†]These authors contributed equally to this work

*nblanke@bu.edu

Abstract: The combination of polarization-sensitive optical coherence tomography (PS-OCT) and birefringence microscopy (BRM) enables multiscale assessment of myelinated axons in postmortem brain tissue, and these tools are promising for the study of brain connectivity and organization. We demonstrate label-free imaging of myelin structure across the mesoscopic and microscopic spatial scales by performing serial-sectioning PS-OCT of a block of human brain tissue and periodically sampling thin sections for high-resolution imaging with BRM. In co-registered birefringence parameter maps, we observe good correspondence and demonstrate that BRM enables detailed validation of myelin (hence, axonal) organization, thus complementing the volumetric information content of PS-OCT.

© 2023 Optica Publishing Group under the terms of the [Optica Open Access Publishing Agreement](#)

1. Introduction

As neurons fire in the brain, axons enable high-speed conduction of the electrical signal from the neuron soma to a distal location, where the neuron forms synaptic connections with other cells. In the central nervous system (CNS), oligodendrocytes are responsible for myelinating axons to increase the speed and energy efficiency of conduction, and they do so by prioritizing axons with larger diameters and higher levels of electrical activity [1,2]. Each neuron has one axon, and put simply, each myelinated axon, or fiber, represents a link in communication between two regions of the brain, or between the brain and other parts of the body. The assessment of fibers and their three-dimensional (3D) orientations within the brain provides a measure of the degree of connectivity between associated regions or the architectural organization within a specific region. Metrics of fiber organization have direct applications in studies of neuroanatomy and tractography.

Myelinated axons can be imaged at several different length scales, ranging from high-resolution imaging of individual axons to imaging of bundles of axons within white matter tracts. For the limits of the range of resolution, there are two established techniques: electron microscopy (EM) and diffusion-weighted magnetic resonance imaging (dMRI). EM provides the highest (<1 nm) resolution images of myelinated axons at the ultrastructural level [3–5], but EM preparations are technically challenging and cannot be used to investigate axonal trajectories over larger spatial scales. On the other hand, dMRI, which measures the anisotropic diffusion of water in brain tissue and can be employed in vivo [6], enables volumetric imaging of bundles of myelinated

axons and their trajectories across any region of the brain, but with mesoscopic resolution (typically ~ 1 mm in vivo or ~ 200 μ m ex vivo). As dMRI contrast is based on local alignment and packing density of axons and their myelin [7–9], dMRI excels for imaging of fiber bundles within white matter tracts [10–12], while it faces resolution and sensitivity limitations in regions with complicated fiber configurations, such as superficial white matter and gray matter [13–16]. For improving dMRI reconstruction algorithms and the interpretation of dMRI data, new methods of microscopic validation are needed [17–19].

For imaging and studying the organization of the brain, label-free optical methods are highly attractive, as they provide direct contrast based on native structures or molecules in tissue. For imaging myelinated axons, specifically, the unique structure and composition of myelin can be leveraged to enable label-free mapping of axonal trajectories. Due to its composition of densely packed lipids and proteins, myelin has a high refractive index, resulting in strong scattering in aqueous media. One of the most promising methods for label-free, volumetric imaging of myelin (as well as cells and vasculature) in brain tissue is optical coherence tomography (OCT), which images scattered light in reflectance and provides depth-resolved intensity contrast based on the density of myelinated axons within a given voxel [20,21].

In addition to its scattering properties, the myelin sheath exhibits strong optical birefringence, a consequence of the anisotropic structure of the lipids [22,23], resulting in anisotropy of the electric polarizability and, hence, the optical index of refraction. Optical birefringence of myelin is imaged using polarized light, and the birefringence is characterized quantitatively by the relative retardance (induced between orthogonal polarization components) and the in-plane optic-axis orientation. As birefringence is directional, birefringence parameters directly facilitate the study of myelinated axons and their spatial organization across brain tissues. Due to the radial orientation of the optic axis of myelin birefringence, when imaging myelinated axons with polarized light, the myelin sheath provides birefringence contrast at its edges (Fig. 1). The tracking of fibers can be readily carried out with birefringence imaging of myelin, as the myelin optic axis and fiber structural axis are always normal to one another.

To extend OCT for the simultaneous detection of myelin birefringence and scattering, polarization-sensitive OCT (PS-OCT) was developed [24], enabling volumetric imaging of fibers in brain tissue with micrometer-level resolution [25]. The fibers are imaged and quantified by their scattering properties and birefringence parameters. When combined with a serial sectioning approach, PS-OCT can be used to image large volumes of brain tissue without distortions due to sectioning and slide preparation [26]. In ex vivo brain tissues, PS-OCT shows great promise for validating fiber orientation distributions predicted by dMRI [19,27]. While PS-OCT excels for mesoscopic imaging of myelin across large volumes of brain tissue, a microscopy approach with higher numerical aperture (NA) is required for imaging myelin at the level of individual axons. High-NA polarization-sensitive optical coherence microscopy (PS-OCM) has been demonstrated [28], but with the use of a coherent light source, there is an inevitable loss of resolution and sensitivity due to laser speckle noise.

To achieve higher resolution images of myelinated axons, but limited to smaller volumes, brain tissue may be sectioned and imaged with birefringence microscopy (BRM) [29]. BRM provides diffraction-limited images of myelin birefringence with any objective, and avoids speckle by utilizing an incoherent, narrowband light source such as a bandpass-filtered lamp or LED. BRM provides either qualitative images of the birefringence in real-time, with cross-circular polarized BRM (CCP-BRM) [30], or quantitative images with quantitative BRM (qBRM) [31]. The main principles of qBRM closely mirror the work and optical setup of Axer *et al.* and their development of “3D polarized light imaging” (3D-PLI) [32], but has not been previously used for high-resolution imaging at single-axon scales. Just as in PS-OCT, qBRM involves the determination of the relative retardance and in-plane optic-axis orientation (birefringence parameters) of myelin. With access to these structural contrasts at higher resolution than PS-OCT,

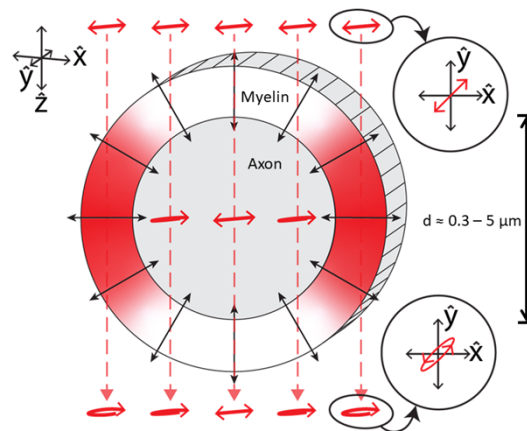


Fig. 1. Birefringence of myelin imaged with polarized light. Cross-sectional diagram of a myelinated axon oriented “longitudinally” within tissue: parallel to the surface of the section (and parallel to the imaging plane). The typical range of diameters for myelinated axons in the CNS ($\sim 0.3\text{--}5\text{ }\mu\text{m}$) is noted on the right side of the diagram. The radial optic axis of myelin is indicated with black arrows. In this illustration, linearly polarized light is incident from above, with its electric-field vector oscillating at 45 degrees to the structural axis of the fiber. Regions of the myelin sheath that generate birefringence contrast are shown with red shading. After propagating through the edges of the myelin sheath, where the myelin optic axis is oriented within the polarization plane, the electric field vector traces out an elliptical pattern. For polarized light propagating through the middle of the myelin sheath, where the myelin optic axis is oriented parallel to the direction of light propagation, there is no change in the incident polarization state.

qBRM can be used to image the same tissue to provide complementary information for validation. However, since qBRM is restricted to thin sections, it is challenged in quantifying large volumes of tissue and is thus complemented by PS-OCT.

In this work, we perform multiscale imaging of a block of human brain tissue with both serial-sectioning PS-OCT and qBRM, and we compare the birefringence parameters extracted with the two methods in various regions of gray and white matter, with an emphasis on regions with crossing fibers. The ability to resolve and validate the orientations of crossing fibers within white matter has gained great attention in the field of dMRI, as these regions with multiple, complex fiber orientations within a voxel are where traditional dMRI (or diffusion tensor imaging) tractography fails to accurately determine orientations unambiguously [11,13,33,34]. The same problem extends to low-resolution polarized-light (birefringence) imaging of white matter regions with crossing fibers, where mixtures of crossing fibers result in attenuation of retardance and the inability to analyze multiple orientations, leading to a misinterpretation of the total distribution of fiber orientations [32,35–37]. With high-resolution qBRM, these challenges can be overcome by acquiring high-resolution z-stacks across the thickness of the brain section. The combined use of PS-OCT and qBRM enables multiscale assessment of myelinated axons and their organization within the human brain, and these complementary tools are promising for the study of connectivity, validation of dMRI, and the characterization of damage to myelinated axons in neurodegenerative diseases.

2. Methods

2.1. Tissue preparation

A block of human brain tissue ($2 \times 2 \times 0.5$ cm) from the dorsolateral prefrontal cortex, sectioned in the coronal plane [Fig. 2(b)], was obtained from the Boston University Alzheimer's Disease Research Center brain bank. The tissue came from a patient with chronic traumatic encephalopathy (CTE, stage III) with a post-mortem interval that did not exceed 24 hours. It was fixed by immersion in 10% formalin for ~2 months, and before preparing the tissue block for imaging, the sample was washed in phosphate-buffered saline (PBS) for a month to ensure complete removal of residual fixative.

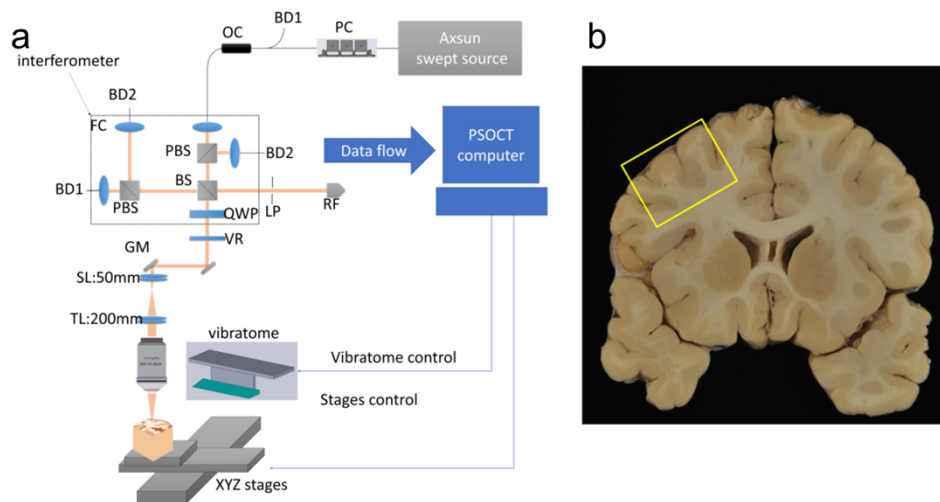


Fig. 2. (a) PS-OCT schematic. (b) Diagram of anatomical region (yellow box) that was imaged in the coronal plane of the dorsolateral prefrontal cortex. OC: optical circulator. PC: polarization controller. BD1-2: two balanced detectors. FC: fiber collimator. PBS: polarized beam splitter. BS: beam splitter. QWP: quarter-wave plate. LP: linear polarizer. RF: retroreflector. VR: variable retarder. GM: Galvo mirror pair. SL: scan lens. TL: tube lens.

To prepare the tissue for imaging with serial-sectioning PS-OCT, the tissue block was embedded in 4.5% agarose for structural support and was then partially index-matched by immersion in a solution of 40% glycerol (60% PBS) for three days. During imaging, the sample was also immersed in 40% glycerol. The concentration of 40% glycerol ($n \approx 1.38$) was chosen to provide partial index-matching to myelin lipids ($n \approx 1.46$) for adequate optical penetration, yet still retaining enough scattering for imaging of backscattered light. Additionally, with the vibratome integrated into our PS-OCT system, we have experienced difficulties with generating reliable tissue sections when using higher glycerol concentrations. Immediately after block-face PS-OCT imaging, the most superficial 150 μm of tissue was cut away from the block in the form of multiple 30 μm coronal sections, and the sections were collected in sequence (in vials of PBS) for high-resolution imaging with qBRM. After cutting away the 150 μm of surface tissue, the next portion of the block was accessible for another PS-OCT image.

For qBRM, each 30- μm brain section was transferred to a shallow dish filled with PBS, and the sections were individually guided onto a gelatin-coated microscope slide with a paintbrush. As myelin structure is highly sensitive to degradation during drying of the tissue (commonly employed as a method for adhering tissue to a slide), care must be taken to avoid lengthy drying steps during slide preparation. After manipulating the brain section as necessary to remove

wrinkles or folds, additional PBS is removed from the section by applying a piece of lint-free optical grade lens tissue directly on the tissue section and leaving it for several seconds. The lens tissue soaks up the majority of the PBS without risk of tissue to lift-off from the gelatin-coated slide when removed. Immediately after removing the lens tissue, the mounting medium (85% glycerol in PBS + 0.01% sodium azide) is pipetted over the brain section and the coverslip is placed on top and sealed with nail polish. The 85% glycerol ($n \approx 1.46$) mounting medium provides optimal index-matching to myelin lipids for minimizing scattering and maximizing birefringence contrast during qBRM.

2.2. Serial-sectioning PS-OCT

The PS-OCT microscope [Fig. 2(a)] was described previously [38]. We use a swept source laser (AxsunTech) with a 100 kHz sweep rate, a central wavelength of 1310 nm, and a spectral full-width-half-maximum (FWHM) of 110 nm, yielding an axial resolution of 7 μm in brain tissue. Imaging is performed with a 4X objective lens (Olympus UPLFLN4X, NA 0.13), providing a lateral resolution of 6 μm and a confocal parameter of 150 μm . We use 1 \times 1 mm field-of-view (FOV) with a 3- μm lateral step size and 30% overlap between tiles. The sample is mounted on XYZ-motorized stages, which translate the sample during imaging of the whole surface and between the vibratome and objective lens. The system invokes a free-space interferometer, with a quarter-wave plate (QWP) and a polarizing beam-splitter to illuminate the sample with circularly polarized light and uses two balanced detectors for measuring orthogonally polarized reflected light. A variable retarder (VR) placed in the sample arm is used to compensate for the system birefringence, enabling precise measurement of sample birefringence [38]. Nevertheless, there is residual birefringence across different regions of the FOV that are a result of scanning the sample with galvo mirrors (GM), as varying angles of incidence on the mirror surface induce slightly different changes to the polarization state that cannot be individually compensated [39]. The GM scanning results in the repetitive green and purple tiling patterns seen in regions of PS-OCT optic-axis orientation maps with low birefringence signal. When using a glass slide for a background measurement of the system, the relative retardance was measured to be less than 5° across the FOV, with the center of the FOV being close to 0°. After block-face imaging, a custom vibratome cuts off 30 μm brain sections for imaging with BRM.

Determination of the scattering coefficient, μ_s [40,41], and birefringence [42] followed previously reported methods, by fitting the depth profiles of PS-OCT intensity and retardance. Briefly, μ_s is extracted by fitting the depth attenuation of OCT signal to the following nonlinear model,

$$R(z) = \mu_b \cdot e^{-2\mu_s z} \cdot PSF(z), \quad (1)$$

where $R(z)$ is the OCT signal as a function of depth, μ_b is the backscattering coefficient and $PSF(z)$ is the point spread function. For extraction of birefringence parameters, PS-OCT measures the orthogonal polarization states of the sample reflection. The relative retardance,

$$\delta = \tan^{-1} \left(\frac{A_1}{A_2} \right), \quad (2)$$

and optic-axis orientation,

$$\varphi = \frac{\phi_1 - \phi_2}{2}, \quad (3)$$

are determined by analyzing the amplitude and phase of the complex signal after taking the Fourier transform of the spectral domain data. In Eqs. (2) and (3), A_1 and A_2 are the amplitude and ϕ_1 and ϕ_2 are the phase of the polarization detection channels, which are parallel and perpendicular to the input polarization, respectively. For the relative retardance maps, Eq. (2) gives the accumulated relative phase retardance, which is integrated over the confocal parameter

(150 μm), where the relative retardance (δ) is the product of the optical birefringence (Δn) and the thickness (t) of an anisotropic tissue, normalized by wavelength (λ):

$$\delta = \frac{\Delta n \cdot t}{\lambda}. \quad (4)$$

In fitting both Eq. (1) and Eq. (4), we use about 200–300 μm of depth and $12 \times 12 \mu\text{m}$ lateral averaging of A-scans. For generation of the optic-axis orientation maps with Eq. (3), we employ the same histogram approach adopted from [28], where the peak φ value is chosen after binning of φ values is performed over pixels in the axial dimension with 5° intervals. We ignored diattenuation effects during the calculation, as absorption is negligible across short distances of fixed brain tissue [43].

2.3. BRM

BRM is a technique that utilizes polarized light to image birefringent structures and is ideally suited for the imaging of myelin with widefield detection at any diffraction-limited optical resolution. In practice, there are two configurations that we use for BRM of myelin [29]. Our custom BRM system (Fig. 3) uses high-speed rotational stages for polarization control and high-speed translation stages to manipulate the sample in XY and the objective in Z (Section S1.1). Real-time imaging is performed with cross-circular-polarized BRM (CCP-BRM), which provides orientation-independent images of birefringence intensity, with myelin generating bright contrast against a dark background. CCP-BRM is user-friendly and convenient for bringing individual axons into focus for visual inspection or for more detailed imaging with quantitative BRM (qBRM). With qBRM, the sample is sequentially illuminated with multiple linear polarization states, and the resulting intensity is detected through a circular analyzer, enabling determination of the birefringence parameters. In unprocessed qBRM images taken with different illuminator polarizer angles, θ , each pixel exhibits a sinusoidal intensity, $I(\theta)$, depending on local birefringence of tissue:

$$I(\theta) = \frac{I_0}{2} [1 + \sin(2(\theta - \varphi)) \cdot \sin(2\pi\delta)], \quad (5)$$

where I_0 is the transmittance, φ is the in-plane optic-axis orientation, and $|\sin(2\pi\delta)|$ is the relative retardance given by Eq. (4). The parameter maps for relative retardance, $|\sin(2\pi\delta)|$, in-plane optic-axis orientation, φ , and transmittance, I_0 , can be determined by utilizing a solution to Eq. (5) with measurements at three values of θ (Section S1.2).

For BRM, the optical resolution is governed by the Abbe diffraction limit, where the lateral resolution,

$$d_{\text{lateral}} = \frac{\lambda}{2 \cdot NA}, \quad (6)$$

and axial resolution,

$$d_{\text{axial}} = \frac{2 \cdot \lambda}{(NA)^2}, \quad (7)$$

are dependent on the wavelength (λ) and the numerical aperture (NA) of the objective lens. Our BRM system incorporates a set of 4X (NA 0.13), 10X (NA 0.3), 20X (NA 0.5), and 40X (NA 0.75) air objectives as well as a 60X oil-immersion (NA 1.35) objective. Depending on the length-scale and features of interest to the user, different objective lenses are chosen. With lower- NA objectives [e.g., 4X (NA 0.13) and 10X (NA 0.3)], the entire thickness of a 30- μm thick brain section is approximately captured within one focal plane, while with higher- NA objectives [e.g., 20X (NA 0.5), 40X (NA 0.75) and 60X (NA 1.35)], volumetric images are acquired across the thickness of the section as z-stacks. As BRM is rapid and imaged with widefield detection (i.e., a camera), BRM acquisitions routinely involve scanning the tissue in a grid-pattern, either

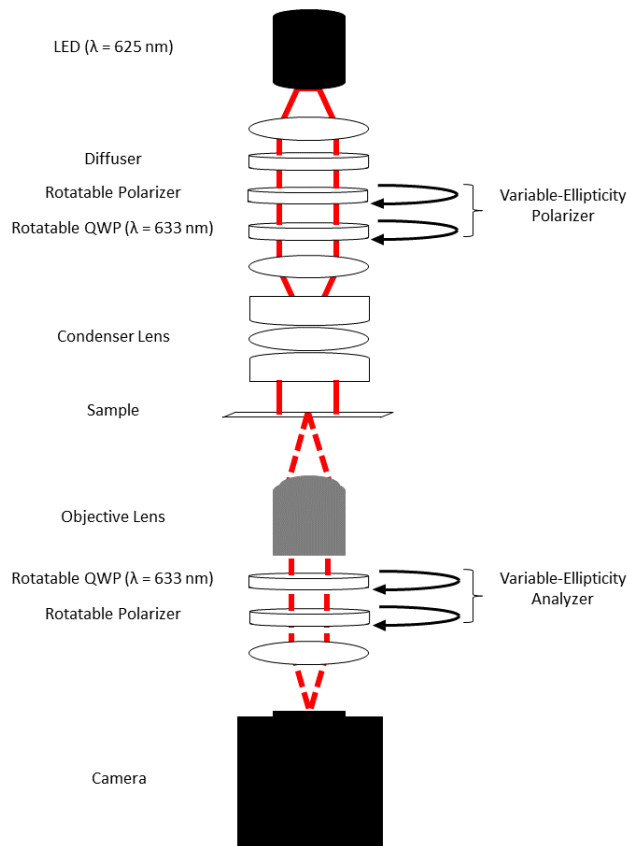


Fig. 3. BRM schematic. The solid red lines indicate illumination rays and the dashed red lines indicate image-forming rays. LED: light-emitting diode. QWP: quarter-wave plate.

over the entire brain section or within designated regions of interest (ROIs), and performing stitching. For displaying and stitching high-resolution BRM images acquired as z-stacks, BRM images are focus-stacked (Section S1.2).

2.4. Coregistration of birefringence parameter maps between PS-OCT and qBRM

Due to the use of different optical systems for imaging, the optic-axis orientation maps of PS-OCT and qBRM required careful alignment in post-processing. First, we rotated the PS-OCT images based on landmarks in the tissue for initial physical alignment of the PS-OCT and 10X qBRM images. We then digitally rotated the PS-OCT orientation data and re-applied the color-wheel to minimize the difference in orientation values across the PS-OCT and 10X qBRM optic-axis orientation maps. For better alignment of the PS-OCT and 20X qBRM images, the PS-OCT zoom-in was physically rotated further, based on landmarks in the tissue (e.g., blood vessels), followed by the corresponding digital rotation to the PS-OCT orientation data. After alignment and digital rotation, the same color-wheel was used for both modalities. Different regions of the tissue required slightly different rotations due to distortions in the slide-mounted brain section that was imaged with qBRM.

2.5. Quantitative analysis of PS-OCT and qBRM images

To quantitatively compare the retardance and optic-axis orientation between PS-OCT and qBRM, we manually selected 0.5×0.5 mm ROIs that were uniformly distributed across white and gray matter at corresponding regions in PS-OCT and qBRM images and calculated the mean retardance and circular mean optic-axis orientation of each ROI. Circular mean was calculated using the MATLAB Circular Statistics toolbox [44]. We then linearly correlated the PS-OCT and qBRM measurements in Origin using the linear fitting tool. We report the residual sum of squares and Pearson's r values as metrics of linear fitting quality.

3. Results

3.1. Multiscale imaging of myelinated axons in brain tissue

PS-OCT and qBRM were used to image myelinated axons across multiple spatial scales in the same human brain tissue. During PS-OCT, the light backscattered from the block of tissue is imaged in a reflectance geometry with $6\text{-}\mu\text{m}$ lateral resolution and $7\text{-}\mu\text{m}$ axial resolution, across the superficial layer of tissue. It should be noted that the spatial resolution of PS-OCT is not sufficient to image details of individual fibers (with diameters of $\sim 0.3\text{ }\mu\text{m}$ to $\sim 5\text{ }\mu\text{m}$), but rather, fiber bundles. In the acquired images of reflectance, the size of each voxel is $3 \times 3 \times 3.5\text{ }\mu\text{m}$, based on the lateral step of the galvo mirrors and the spectral range of the illumination source. For determining parameter maps with PS-OCT, the reflectance signal is analyzed across multiple voxels in depth, providing final depth-resolved measurements of scattering and retardance slope over intervals of $150\text{ }\mu\text{m}$ in depth. Additionally, due to imaging with a coherent light source, 4×4 spatial averaging is required to remove laser speckle noise from the images. As a result, the size of a PS-OCT voxel shown within an image is $12 \times 12 \times 150\text{ }\mu\text{m}$. With the serial-sectioning approach, volumetric maps of scattering, retardance, and in-plane optic-axis orientation were obtained for the entire block of tissue at this voxel size.

For qBRM, individual $30\text{-}\mu\text{m}$ sections are taken while performing serial sectioning, to be imaged with diffraction-limited resolution (up to a lateral resolution of $\sim 250\text{ nm}$) in a transmission microscope. Depending on the NA of the objective lens used during qBRM, the $30\text{-}\mu\text{m}$ thick section is either imaged through the entire thickness dimension at once, or with multiple planes as a z-stack. In this work, two objective lenses were used for imaging: 10X (NA 0.3) for low-resolution, whole-section images and 20X (NA 0.5) for high-resolution images of individual myelinated axons in particular ROIs. With red light ($\lambda = 625\text{ nm}$), the lateral resolution of qBRM is $\sim 1\text{ }\mu\text{m}$ for the low-resolution (10X) images and $\sim 0.6\text{ }\mu\text{m}$ for the high-resolution (20X) images, while approximate values for axial resolution are $\sim 14\text{ }\mu\text{m}$ and $\sim 5\text{ }\mu\text{m}$ for low- and high-resolution, respectively. For high-resolution imaging within relatively thick ($30\text{ }\mu\text{m}$) brain sections, the increased lateral resolution helps for resolving individual myelinated axons, but the biggest difference in resolving power is afforded by the increased axial resolution of the higher-NA objective, as axial resolution is proportional to the inverse square of the NA. High-resolution qBRM requires z-stack imaging, as each image is constrained to a specific imaging plane within the tissue section.

A direct comparison of PS-OCT and 10X qBRM images, across the entire sample and from the same volume of tissue, are shown in Fig. 4. The images shown are the relative retardance [Fig. 4(a) and (d)], the in-plane optic-axis orientation [Fig. 4(b) and (e)], and optical scattering/transmittance [Fig. 4(c) and (f)]. The PS-OCT images [Fig. 4(a)–(c)] are acquired over $150\text{ }\mu\text{m}$ of depth, while the qBRM images [Fig. 4(d)–(f)] are acquired from one $30\text{-}\mu\text{m}$ thick section. Regardless of some missing tissue in the gray matter of PS-OCT images, which was a result of peeling away pial vessels at the cortical surface (to provide reliable sectioning), the PS-OCT images are free from distortion. During slide preparation for qBRM, however, there were several occurrences of slight tearing and distortion of the section, which can be seen most prominently at the cortical surface

and in gray matter. The images in Fig. 4 demonstrate that we achieved accurate co-registration of birefringence parameter maps, as well as the scattering and transmittance maps, imaged with each method. The birefringence parameter maps (relative retardance and optic-axis orientation) are expected to convey the same information, even though they are imaged across slightly different volumes, while the scattering maps convey slightly different information, due to the fact that optical scattering is being measured with different configurations (reflectance for PS-OCT and transmission for qBRM).

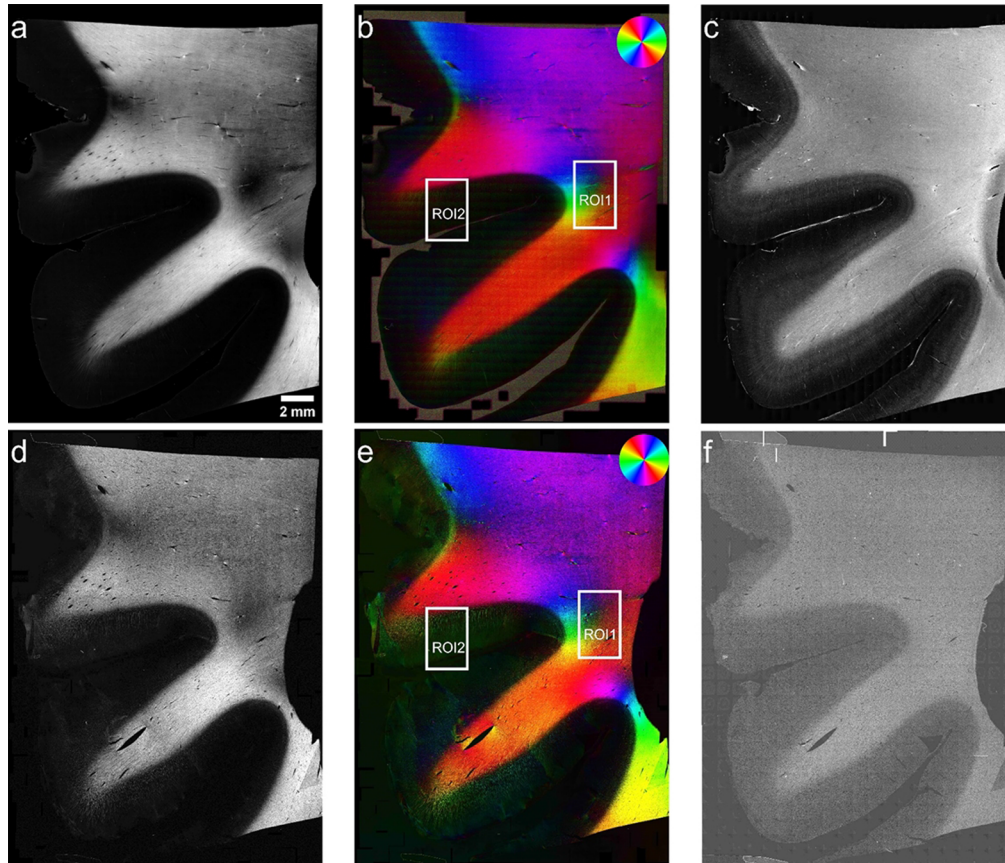


Fig. 4. PS-OCT and low-resolution qBRM images from a block of human brain tissue. The qBRM images were acquired with a 10X (NA 0.3) objective. Top row: PS-OCT. Bottom row: qBRM. (a) PS-OCT relative retardance. (b) PS-OCT in-plane optic-axis orientation. (c) PS-OCT scattering (μ_s). (d) qBRM relative retardance. (e) qBRM in-plane optic-axis orientation. (f) qBRM transmittance (inverted). The color-wheel in the top-right corner of (b) and (e) indicates the direction of the myelin optic axis, which is orthogonal to the axis of the axonal tract. ROIs 1 and 2, denoted in (b) and (e), are further analyzed in Fig. 6 and Fig. 7.

In the retardance maps [Fig. 4(a) and (d)], we observe the same patterns of darkening within white matter regions, which are due to crossing fibers, through-plane (inclined) fibers, or regions where white matter density reduces (i.e., gray matter transitions) [32,35]. Regions of crossing fibers appear darker than the surrounding white matter due to cancellation of retardance from orthogonally oriented birefringent structures, while through-plane fibers appear darker because they are azimuthally symmetric in cross-section, with the full range of optic-axis orientations

along their edges, therefore also resulting in cancellation of retardance when imaged at low resolution. With access to isotropic scattering contrast in OCT [Fig. 4(c)] in the same regions where darkening is observed, it is straightforward to rule out the darkening happening as a reduction in myelin density [45]. With only the PS-OCT images, it is difficult to assess if the dark regions are primarily due to crossing or through-plane fibers, as both reduce the in-plane anisotropy. However, with high-resolution qBRM, these regions can be imaged in detail to directly reveal the orientations of the fiber population at the level of individual axons (Section 3.2).

In the optic-axis orientation maps [Fig. 4(b) and (e)], there is good agreement between the PS-OCT and qBRM images. Small mismatches in orientations [e.g., at the bottom portion of the qBRM image in Fig. 4(e)] can be attributed to distortions in the tissue during sectioning or slide preparation for qBRM. When viewing these orientation maps, with the expectation of mapping fiber directions, the longitudinal orientations of axons appear at 90° to the colors of the orientation wheel inset, due to the optic axis of myelin (Fig. 1) being normal (radial) to the fiber axis. For users interested in a visual cue for mapping the directions of fibers across the tissue, the color-wheel can simply be rotated by 90° , and the color-wheel would then be viewed as a map of fiber projections.

In the scattering maps [Fig. 4(c) and (f)], the clear distinction between gray and white matter regions is conserved between the two methods. The PS-OCT image [Fig. 4(c)] is a map of isotropic scattering (μ_s), measured in reflectance, while the qBRM image [Fig. 4(f)] is a map of intensity loss during transmission through the sample (transmittance). The qBRM transmittance map is inverted to match the PS-OCT scattering map. In the absence of absorption, which can be assumed to be negligible over these short distances and at these wavelengths in fixed brain tissue, the inverted transmittance map provides a readout of optical scattering. This scattering signal, however, is not isotropic and has been shown to be highly sensitive to the inclination angle of fibers within white matter [37,46]. As a result, we do not expect there to be a universal one-to-one correspondence between these two maps within any brain region. Additionally, for qBRM, there is a practical motivation to minimize optical scattering from myelin (by performing index-matching with 85% glycerol), as optical scattering from myelin reduces the contrast of birefringence imaging and degrades image quality for investigation of individual fibers. In PS-OCT, on the other hand, optical scattering from myelin is required to measure birefringence in its reflectance geometry, so the scattering signal cannot be optimally minimized (partial index-matching with 40% glycerol).

To quantitatively compare the qBRM and PS-OCT images, we manually selected ROIs across the whole image and analyzed their correlation. Figure 5 shows the quantitative comparison of PS-OCT and qBRM measurements of retardance and optic-axis orientation. In white matter, we observed a strong linear correlation between qBRM and PS-OCT for both retardance [Fig. 5(a)] and optic-axis orientation [Fig. 5(b)] measurements, which confirms that PS-OCT accurately measures optic axis and birefringence properties in regions with a high degree of birefringence. The slope in Fig. 5(b) is very close to one, demonstrating excellent agreement in optic-axis orientation. The plot for relative retardance in Fig. 5(a) also demonstrates very good agreement, but the slope does not have a physical meaning because PS-OCT and qBRM are each imaging across different distances in tissue (and with different NA) and are therefore not expected to yield the same absolute units of phase retardance. For either method, leaving the maps of relative retardance in arbitrary units is equally as valid as assigning absolute units, as the images are simply intended to provide visualization of relative changes in myelination across different regions of tissue. Furthermore, it is difficult to relate an absolute measure of optical retardance back to a meaningful measure of myelin content, without significant assumptions about the alignment of the fibers across the imaging volume. While qBRM may still be required for high-resolution

visualization of individual fibers, PS-OCT provides reliable images of myelin birefringence at the mesoscopic scale within white matter.

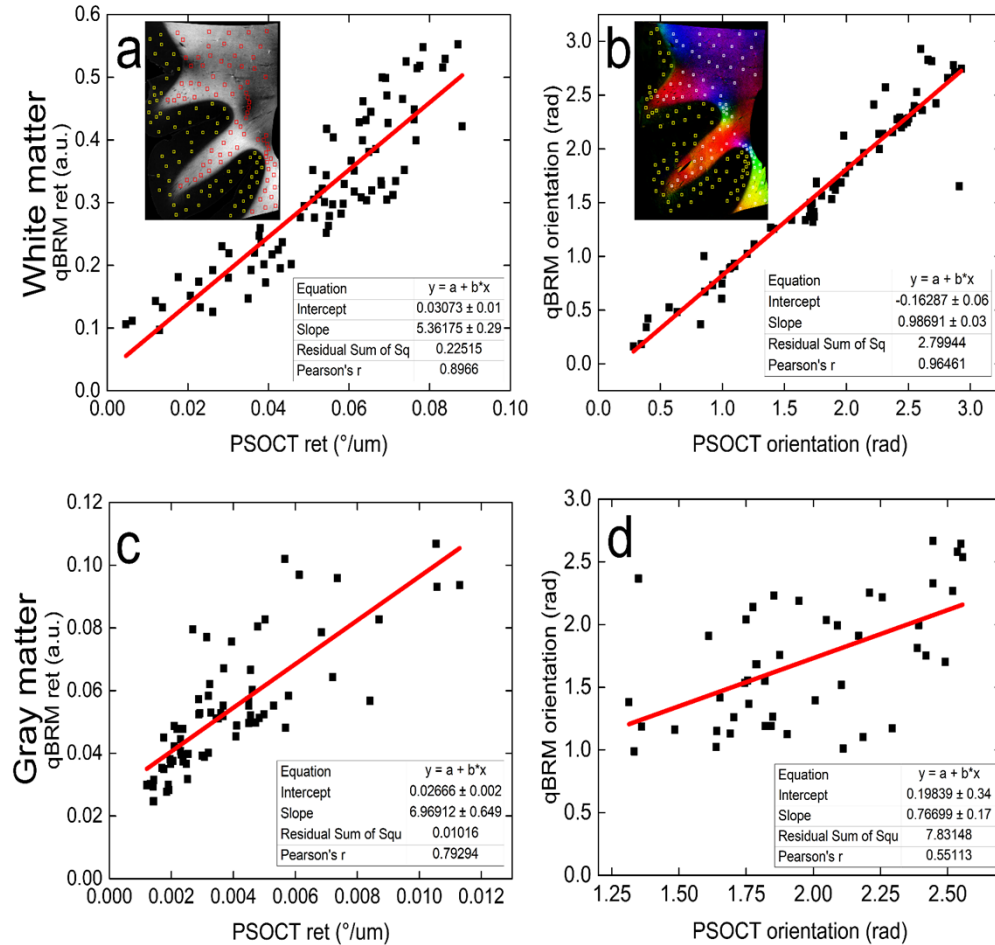


Fig. 5. Quantitative analysis between coregistered PS-OCT and qBRM images. (a) White matter qBRM retardance vs. PS-OCT retardance. (b) White matter qBRM optic-axis orientation vs. PS-OCT optic-axis orientation. (c) Gray matter qBRM retardance vs. PS-OCT retardance. (d) Gray matter qBRM optic-axis orientation vs. PS-OCT optic-axis orientation. The ROIs used to generate these plots are overlaid on the qBRM images in the inset of (a) and (b).

In gray matter regions, the correlations were weaker. In the correlation plot for relative retardance of gray matter [Fig. 5(c)], we observed higher error in regions with higher retardance, which is likely due to the imperfect coregistration between the two modalities during ROI selection. PS-OCT images were taken across 150 μm in depth and were free from distortions, while qBRM images were taken from a 30- μm section that suffered slight distortions during slide preparation. As a result, when comparing birefringence parameters from slightly different volumes of tissue in the PS-OCT and qBRM images, there are ROIs that contain slightly different fiber populations. Since the regions of gray matter that have the highest retardance also have the largest number of fibers, these regions are more susceptible to variability in the fiber populations that were captured. In gray matter regions with lower retardance, there are less fibers altogether, so these regions were less susceptible to variability. For optic-axis orientation measurements in gray matter [Fig. 5(d)],

we only analyzed the infragranular layers, since the PS-OCT signal in the supragranular layers was largely contaminated by system bias (Section 2.2). In the infragranular layers of gray matter, PS-OCT measurements of optic-axis orientation are correlated with qBRM, but expectedly with a weaker correlation than in white matter. These data suggest that high-resolution qBRM is necessary for the investigation of the organization and optic-axis orientations of fibers in gray matter.

3.2. *qBRM enables validation of PS-OCT optical property maps at the level of individual myelinated axons*

Two regions that appeared to comprise crossing fibers were selected for high-resolution qBRM, to illustrate how qBRM provides individual-fiber validation of PS-OCT images from the same human brain section. With a high-NA objective, multiple fiber orientations can be resolved in qBRM for each PS-OCT voxel. Figure 6 shows the PS-OCT and qBRM images of subcortical white matter [ROI 1 in Fig. 4(b) and (e)], where there are multiple distinct fiber directions converging together, indicated by the different orientation colors. In the coregistered optic-axis orientation maps determined with PS-OCT [Fig. 6(a)] and high-resolution qBRM [Fig. 6(b)], there are polar plot overlays that provide a visualization of the major direction and distribution of local fiber orientations. The colors of the polar plots indicate the major directions of the myelin optic axis, while the spread of the polar plots represents the diversity of corresponding fiber orientations measured in that local area. Crossing fibers exist at all locations of this ROI, especially at the center where the polar plot is widest. Across the PS-OCT and qBRM optic-axis orientation maps, we observed an overall correspondence between the major directions and the relative spreads of the polar plots, confirming that PS-OCT provides correct mapping of the major fiber orientations, validated with high-resolution qBRM. However, as expected, high-resolution qBRM demonstrated more sensitivity to the variety of non-major fiber orientations, indicated by the slightly wider polar plot distributions relative to PS-OCT.

Figure 6(c) shows the cropped and zoomed region with the widest polar plot distribution of orientations [indicated by the white box in Fig. 6(a) and (b)], demonstrating that qBRM provides detailed images of individual fibers and their orientations, while PS-OCT [Fig. 6(e)] shows less detail of the same fibers. Within this region, there is a high degree of crossing fibers and, effectively, no through-plane fibers. In similar white matter regions of other brain sections, where we see crossing fibers, it is common to also see a population of through-plane fibers, which, due to the radial optic axis of myelin (Fig. 1), appear as circular cross-sections with the full range of the color-wheel around their circumference [see blue arrow in Fig. 7(c)]. In an expanded view of the high-resolution qBRM orientation map [Fig. 6(d)], an example of a through-plane blood vessel (blue asterisk) within white matter can be seen in the lower left, where myelinated axons wrapping around the blood vessel also display the full range of the orientation color-wheel.

The cortex and superficial white matter are also rich in distinct crossing fiber populations, where there are “radial” fibers extending perpendicular to the surface of cortex and “horizontal” fibers running parallel to the surface of the cortex [47,48]. Figure 7 shows the PS-OCT and qBRM images acquired within a cortical region at the crest of a gyrus [ROI 2 in Fig. 4(b) and (e)]. In the optic-axis orientation maps imaged with PS-OCT [Fig. 7(a)] and high-resolution qBRM [Fig. 7(b)], we observed good correspondence at the mesoscopic scale, and the methods have similar sensitivity to larger bundles of radial fibers extending into the cortex [highlighted by the red arrows in Fig. 7(a) and (b)].

The zoomed-in region indicated by the white box in [Fig. 7(a) and (b)] confirms that high-resolution qBRM [Fig. 7(c)] provides detailed images of both radial (red arrows) and horizontal fibers (white arrows), while only the large bundles of radial fibers (red arrows) are resolved with PS-OCT [Fig. 7(e)]. The horizontal fibers are difficult to distinguish in the PS-OCT optic-axis orientation map, because the small-diameter horizontal fibers are not grouped in

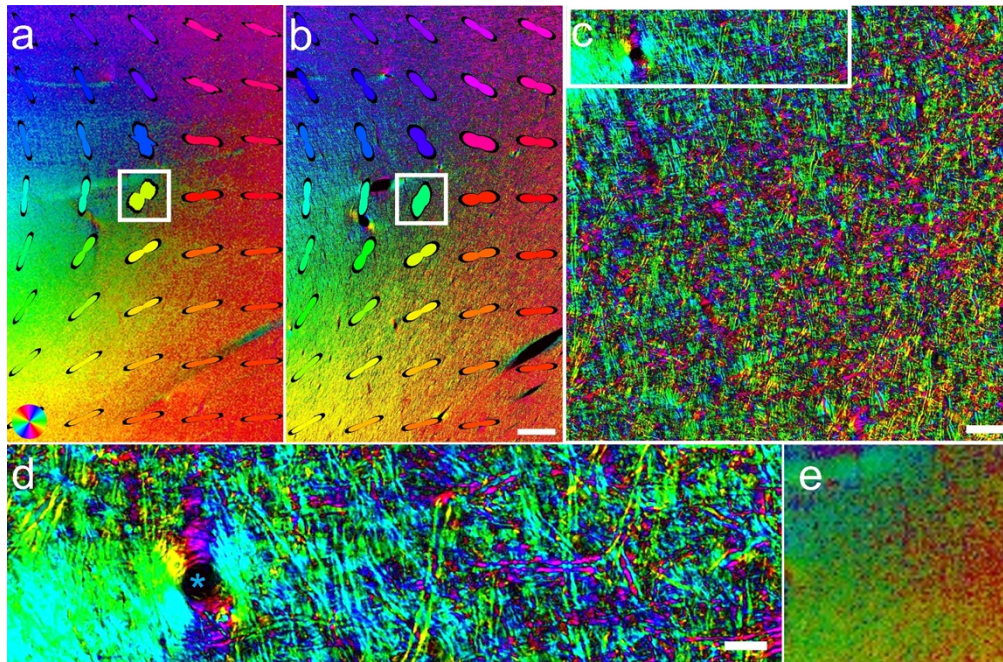


Fig. 6. Quantitative comparison of PS-OCT and high-resolution qBRM in a white matter region with crossing fibers. The region within the full sample is denoted by ROI 1 in Fig. 4. (a) PS-OCT optic-axis orientation with overlaid polar plots. The color-wheel in the lower-left corner indicates the direction of the myelin optic axis in all the images. The polar plot overlays (plotted for image segments of $600 \times 600 \mu\text{m}$) indicate the major optic-axis orientation by color and the variety of local orientation by spread. (b) qBRM optic-axis orientation with overlaid polar plots. The qBRM images were acquired with a 20X (NA 0.5) objective as z-stacks and were focus-stacked before stitching. (c) Zoomed-in region of the qBRM image in (b) indicated by the white box. (d) Zoomed-in region of the qBRM image in (c) indicated by the white rectangle. A through-plane blood vessel with myelinated axons wrapped around it is seen in the lower-left (blue asterisk). (e) Zoomed-in region of the PS-OCT image in (a). Scale bars: (b) $400 \mu\text{m}$, (c) $50 \mu\text{m}$, (d) $20 \mu\text{m}$.

bundles, and because the PS-OCT system has an optical systematic bias that appears as repetitive green and purple stripes across low-signal gray matter regions (Section 2.2). In the top-right portion of the high-resolution qBRM image [Fig. 7(c)], a through-plane fiber (blue arrow) and another through-plane blood vessel [blue asterisk, similar to that in Fig. 6(d)], are indicated for comparison. Even though qBRM is only performed in 2D, high-resolution, z-stacks provide the ability to estimate the 3D-orientation of through-plane fibers and inclined fibers. When zooming in on the cortical surface [Fig. 7(d)] of the section within the qBRM image [indicated by the white rectangle at the bottom of Fig. 7(b)], layers I and II of the cortex can be identified by the resolved individual horizontal fibers (white arrows). With PS-OCT, these layers and the fibers within them are difficult to visualize due to the fibers being small-diameter and because of the system bias noted previously. As a side note, the yellow dots seen throughout Fig. 7(d), and in other regions of the qBRM images of the cortex, are due to scattering from structures in the tissue (i.e., blood vessels, cells, axons and dendrites) and the system correction employed during qBRM image analysis (Section S1.3).

In summary, we have demonstrated that PS-OCT, which can image large tissue volumes, correctly generates mesoscopic-scale retardance and optic-axis orientation maps in gray and

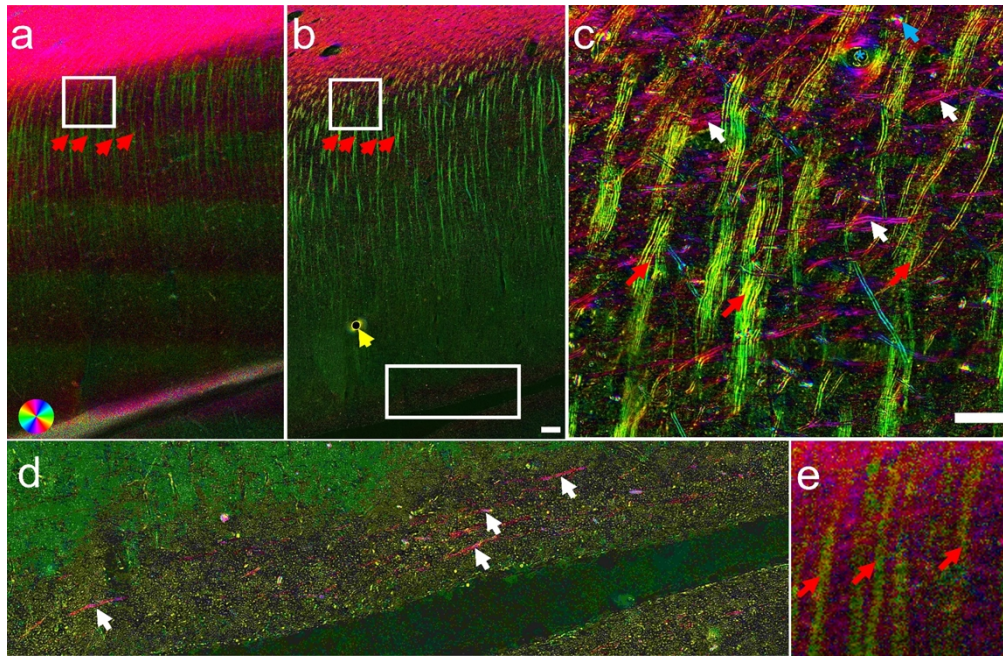


Fig. 7. Comparison of PS-OCT and high-resolution qBRM in a cortical region with crossing fibers. The region within the full sample is denoted by ROI 2 in Fig. 4. (a) PS-OCT optic-axis orientation. The color-wheel in the lower-left corner indicates the direction of the myelin optic axis in all the images. The red arrows highlight radial fibers captured in both modalities. (b) qBRM optic-axis orientation. The qBRM images were acquired with a 20X (NA 0.5) objective as z-stacks and were focus-stacked before stitching. The yellow arrow highlights an air bubble situated in a through-plane blood vessel, which is given a yellow color due to scattering and the system correction employed during qBRM image analysis (Section S1.3). (c) Zoomed-in region of the white square from the qBRM image in (b). Red arrows point to radial fibers and white arrows point to horizontal fibers. The blue arrow indicates a through-plane fiber, and the blue asterisk indicates a through-plane blood vessel. (d) Zoomed-in region of the white rectangle from the qBRM image in (a), which is in the layer I/II of the cortex. Horizontal fibers are highlighted by white arrows. (e) Zoomed-in region of the white square from the PS-OCT image in (a). Red arrows indicate radial fibers. Scale bars: (b) 200 μm , (c) 50 μm .

white matter, validated with high-resolution qBRM. While individual myelinated axons are beyond the resolution limit of PS-OCT, this is typically not a major concern when studying white matter, as fiber tracts tend to organize in larger bundles. Furthermore, the residual system instrumental bias of birefringence for PS-OCT is not a major limiting factor in white matter, where the birefringence contrast is high. PS-OCT provides unmatched volumetric imaging of white matter, which would be laborious to perform with qBRM of individually sectioned and slide-mounted brain sections. qBRM, on the other hand, is suitable for determination of fiber orientations within dense white matter or sparse gray matter. As qBRM can be applied at low- or high-resolution, and is effective in regions where PS-OCT is limited, qBRM can be used to address the main limitations of PS-OCT. These two techniques are highly complementary when studying the connectivity and organization of the human brain.

4. Discussion

In the study of neuroanatomy, there is tremendous interest in determining and mapping axonal connections across the brain [49]. A more robust understanding of how different regions of the brain communicate with one another can lead to new insights into brain function in health and disease. While dMRI has revolutionized the assessment of connectivity across the whole brain, both in vivo and ex vivo, the limited spatial resolution prevents researchers from obtaining the “full picture” in regions of the brain that exhibit complex combinations of fiber orientations (e.g., regions with crossing and turning fibers). There is a need for methods that can provide complementary imaging of brain architecture at the mesoscopic and microscopic scales, for validation of diffusion metrics and for the determination of ground-truth orientations of fibers in various, complex brain regions. In this work, we demonstrate that, with pure optical contrast, label-free imaging of myelin with both PS-OCT and qBRM provides a powerful and convenient method for studying the structural organization of fibers in the human brain.

We envision an approach to mapping of brain connectivity within postmortem tissues, utilizing serial-sectioning PS-OCT for large-scale, volumetric imaging, with qBRM offering high-resolution validation of fiber orientations within sections generated during PS-OCT imaging. Other current methods for high-resolution imaging of fibers in brain sections include fluorescent staining of myelin and confocal microscopy [50–53], immunohistochemical labeling of myelin proteolipid protein [36] or neurofilament (axons) [54], spectral confocal reflectance (SCoRe) microscopy [55], coherent anti-Stokes Raman scattering (CARS) microscopy [56–58] and two-photon autofluorescence of myelin [59,60]. For the quantitative determination of fiber orientation, these techniques all rely on post-processing analysis of image features, such as structure tensor. With the ability to acquire rapid, widefield images of myelin structure with label-free qBRM, we offer a powerful method for high-resolution determination of individual fiber orientations, compared to those high-resolution microscopy techniques that are time-consuming due to volumetric imaging by point-scanning. The images provided in Fig. 6 and Fig. 7 show the promising capabilities of qBRM for serving as an advantageous method for studying new anatomy and pathology, and for validating PS-OCT and dMRI in any region of the brain, especially those with complex mixtures of fibers. While our qBRM system does not inherently measure the out-of-plane (inclination) angles of fibers, with high-resolution z-stacks taken with qBRM, the 3D propagation of fibers along the thickness of the section can be visualized directly and their 3D angle can be deduced. The transmittance information also offers the potential to aid in the determination of fiber inclination angles [46].

For imaging of fiber orientations at more mesoscopic scales, where fibers are not resolved individually, serial-sectioning PS-OCT offers the unique advantage of enabling volumetric assessment of brain tissue with minimal human intervention. Currently, the main limitation of PS-OCT for this application is that, despite its volumetric imaging capabilities, the birefringence and scattering parameters are restricted to 2D detection, as PS-OCT only measures the projection of fiber orientation on the imaging plane. Measurement of 3D optic-axis orientations has been reported by PS-OCT with multiple illumination angles [61–65] and has been tested on birefringent tissues such as tendon. One important future direction is to further develop the method to reveal the 3D optic-axis orientations of fibers in the brain. Other groups have demonstrated 3D imaging of fibers in brain tissue with myelin birefringence as the contrast mechanism, with the aforementioned 3D-PLI [32,66], and optical scattering as the contrast mechanism, with the more recently developed “scattered light imaging” (SLI) [67,68]. 3D-PLI utilizes the same optical setup as qBRM but is applied at lower resolution and with a tilting stage, which enables determination of the fiber inclination angle. SLI is based on a principle similar to 3D-PLI, but instead of tilting the sample, illumination is performed with multiple angles of incidence, to image scattering anisotropy from fibers in 3D. Both 3D-PLI and SLI are promising for mesoscopic-scale imaging of 3D fiber orientations in white matter, but they are restricted to imaging relatively

thin brain sections, ultimately limiting their ability to be used in larger-scale investigations of brain structure. For PS-OCT, on the other hand, with the use of block-face imaging and serial sectioning, large blocks (up to $\sim 4 \times 4 \times 2$ cm) of brain tissue can be imaged without distortions, making co-registration to dMRI more feasible than it would be for a technique that requires thin sections for imaging.

In conclusion, with the modalities of PS-OCT and qBRM, we have demonstrated multiscale, label-free imaging of myelin and its structural birefringence, providing detailed quantitative images of fiber directionality and organization within the same human brain tissue. PS-OCT and qBRM are inherently complementary to one another, being sensitive to the same birefringence parameters at the mesoscopic and microscopic scales, respectively. Serial-sectioning PS-OCT is superior for preservation of imaging volumes and for pushing the limit on the size of brain tissue blocks that can be imaged within a reasonable time, while qBRM enables widefield and efficient imaging of individual fibers with diffraction-limited resolution up to ~ 250 nm. For validation of dMRI, PS-OCT provides reliable images of fiber-bundle orientations within a volume context, while high-resolution qBRM can be used for unambiguous determination of single-fiber orientations in regions of the brain with sparse fibers or complex distributions of fiber orientations. Together, PS-OCT and qBRM provide a robust toolset for quantifying myelin anisotropy across the postmortem brain.

Funding. National Institute of Biomedical Imaging and Bioengineering (R00-EB023993); Division of Graduate Education (DGE-1633516); National Institute of Mental Health (U01-MH117023); National Institute on Aging (R01-AG075727).

Acknowledgements. The authors would like to thank the Boston University Alzheimer's Disease Research Center for providing the human brain tissues used in this study and the Boston University Neurophotonics Center for support.

Disclosures. The authors declare no conflicts of interest.

Data availability. Data underlying the results presented in this study are available from the corresponding author upon reasonable request.

Supplemental document. See [Supplement 1](#) for supporting content.

References

1. K. A. Nave and H. B. Werner, "Myelination of the nervous system: Mechanisms and functions," *Annu. Rev. Cell Dev. Biol.* **30**(1), 503–533 (2014).
2. C. Stadelmann, S. Timmler, A. Barrantes-Freer, and M. Simons, "Myelin in the central nervous system: Structure, function, and pathology," *Physiol. Rev.* **99**(3), 1381–1431 (2019).
3. A. Peters and C. Sethares, "Aging and the myelinated fibers in prefrontal cortex and corpus callosum of the monkey," *J. Comp. Neurol.* **442**(3), 277–291 (2002).
4. S. Mikula, J. Binding, and W. Denk, "Staining and embedding the whole mouse brain for electron microscopy," *Nat. Methods* **9**(12), 1198–1201 (2012).
5. H. H. Lee, K. Yaros, J. Veraart, J. L. Pathan, F. X. Liang, S. G. Kim, D. S. Novikov, and E. Fieremans, "Along-axon diameter variation and axonal orientation dispersion revealed with 3D electron microscopy: implications for quantifying brain white matter microstructure with histology and diffusion MRI," *Brain Struct. Funct.* **224**(4), 1469–1488 (2019).
6. P. J. Basser, J. Mattiello, and D. LeBihan, "MR diffusion tensor spectroscopy and imaging," *Biophys. J.* **66**(1), 259–267 (1994).
7. S. K. Song, S. W. Sun, M. J. Ramsbottom, C. Chang, J. Russell, and A. H. Cross, "Dysmyelination revealed through MRI as increased radial (but unchanged axial) diffusion of water," *NeuroImage* **17**(3), 1429–1436 (2002).
8. A. L. Alexander, J. E. Lee, M. Lazar, and A. S. Field, "Diffusion Tensor Imaging of the Brain," *Neurotherapeutics* **4**(3), 316–329 (2007).
9. D. Le Bihan, "Looking into the functional architecture of the brain with diffusion MRI," *Nat. Rev. Neurosci.* **4**(6), 469–480 (2003).
10. S. Mori, B. J. Crain, V. P. Chacko, and P. C. M. van Zijl, "Three-Dimensional Tracking of Axonal Projections in the Brain by Magnetic Resonance Imaging," *Ann. Neurol.* **45**(2), 265–269 (1999).
11. Y. Assaf and O. Pasternak, "Diffusion tensor imaging (DTI)-based white matter mapping in brain research: A review," *J. Mol. Neurosci.* **34**(1), 51–61 (2008).
12. V. J. Wedeen, D. L. Rosene, R. Wang, G. Dai, F. Mortazavi, P. Hagmann, J. H. Kaas, and W.-Y. I. Tseng, "The Geometric Structure of the Brain Fiber Pathways," *Science* **335**(6076), 1628–1634 (2012).

13. S. Mori and P. C. M. Van Zijl, "Fiber tracking: Principles and strategies - A technical review," *NMR Biomed.* **15**(7-8), 468–480 (2002).
14. C. Reveley, A. K. Seth, C. Pierpaoli, A. C. Silva, D. Yu, R. C. Saunders, D. A. Leopold, and F. Q. Ye, "Superficial white matter fiber systems impede detection of long-range cortical connections in diffusion MR tractography," *Proc. Natl. Acad. Sci. U. S. A.* **112**(21), E2820–E2828 (2015).
15. K. Schilling, Y. Gao, V. Janve, I. Stepniewska, B. A. Landman, and A. W. Anderson, "Confirmation of a gyral bias in diffusion MRI fiber tractography," *Hum. Brain Mapp.* **39**(3), 1449–1466 (2018).
16. A. Roebroeck, K. L. Miller, and M. Aggarwal, "Ex vivo diffusion MRI of the human brain: Technical challenges and recent advances," *NMR Biomed.* **32**, 1–14 (2019).
17. T. B. Dyrby, G. M. Innocenti, M. Bech, and H. Lundell, "Validation strategies for the interpretation of microstructure imaging using diffusion MRI," *NeuroImage* **182**, 62–79 (2018).
18. A. Lazari and I. Lipp, "Can MRI measure myelin? Systematic review, qualitative assessment, and meta-analysis of studies validating microstructural imaging with myelin histology," *NeuroImage* **230**, 117744 (2021).
19. A. Yendiki, M. Aggarwal, M. Axer, A. F. D. Howard, A. M. V. C. van Walsum, and S. N. Haber, "Post mortem mapping of connectional anatomy for the validation of diffusion MRI," *NeuroImage* **256**, 119146 (2022).
20. H. Wang, M. K. Al-Qaisi, and T. Akkin, "Polarization-maintaining fiber based polarization-sensitive optical coherence tomography in spectral domain," *Opt. Lett.* **35**(2), 154 (2010).
21. C. Magnain, J. C. Augustinack, M. Reuter, C. Wachinger, M. P. Frosch, T. Ragan, T. Akkin, V. J. Wedeen, D. A. Boas, and B. Fischl, "Blockface histology with optical coherence tomography: A comparison with Nissl staining," *NeuroImage* **84**, 524–533 (2014).
22. R. S. Bear, F. O. Schmitt, and J. Z. Young, "The sheath components of the giant nerve fibres of the squid," *Proc. R. Soc. London. Ser. B - Biol. Sci.* **123**, 496–504 (1937).
23. B. de Campos Vidal, M. L. S. Mello, A. C. Caseiro-Filho, and C. Godo, "Anisotropic properties of the myelin sheath," *Acta Histochem.* **66**(1), 32–39 (1980).
24. J. F. de Boer, T. E. Milner, M. J. C. van Gernert, and J. S. Nelson, "Two-Dimensional birefringence imaging in biological tissue using phase and polarization sensitive optical coherence tomography," *Opt. Lett.* **22**(12), 934 (1997).
25. H. Wang, A. J. Black, J. Zhu, T. W. Stigen, M. K. Al-Qaisi, T. I. Netoff, A. Abosch, and T. Akkin, "Reconstructing micrometer-scale fiber pathways in the brain: Multi-contrast optical coherence tomography based tractography," *NeuroImage* **58**(4), 984–992 (2011).
26. H. Wang, C. Magnain, R. Wang, J. Dubb, A. Varjabedian, L. S. Tirrell, A. Stevens, J. C. Augustinack, E. Konukoglu, I. Aganj, M. P. Frosch, J. D. Schmahmann, B. Fischl, and D. A. Boas, "as-PSOCT: Volumetric microscopic imaging of human brain architecture and connectivity," *NeuroImage* **165**, 56–68 (2018).
27. R. Jones, G. Grisot, J. Augustinack, C. Magnain, D. A. Boas, B. Fischl, H. Wang, and A. Yendiki, "Insight into the fundamental trade-offs of diffusion MRI from polarization-sensitive optical coherence tomography in ex vivo human brain," *NeuroImage* **214**, 116704 (2020).
28. H. Wang, T. Akkin, C. Magnain, R. Wang, J. Dubb, W. J. Kostis, M. A. Yaseen, A. Cramer, S. Sakadžić, and D. Boas, "Polarization sensitive optical coherence microscopy for brain imaging," *Opt. Lett.* **41**(10), 2213 (2016).
29. N. Blanke, V. Go, D. L. Rosene, and I. J. Bigio, "Quantitative birefringence microscopy for imaging the structural integrity of CNS myelin following circumscribed cortical injury in the rhesus monkey," *Neurophotonics* **8**(01), 1–15 (2021).
30. R. Schnabel, "Zur mikroskopischen Untersuchung optische anisotroper Strukturen des Nervensystems mit circular polarisiertem Licht," *Acta Neuropathol.* **7**(2), 180–184 (1966).
31. A. M. Glazer, J. G. Lewis, and W. Kaminsky, "An automatic optical imaging system for birefringent media," *Proc. R. Soc. Lond. A* **452**(1955), 2751–2765 (1996).
32. M. Axer, K. Amunts, D. Grässel, C. Palm, J. Dammers, H. Axer, U. Pietrzyk, and K. Zilles, "A novel approach to the human connectome: Ultra-high resolution mapping of fiber tracts in the brain," *NeuroImage* **54**(2), 1091–1101 (2011).
33. H. Oouchi, K. Yamada, K. Sakai, O. Kizu, T. Kubota, H. Ito, and T. Nishimura, "Diffusion anisotropy measurement of brain white matter is affected by voxel size: Underestimation occurs in areas with crossing fibers," *Am. J. Neuroradiol.* **28**(6), 1102–1106 (2007).
34. S. Jbabdi and H. Johansen-Berg, "Tractography: Where Do We Go from Here?" *Brain Connect.* **1**(3), 169–183 (2011).
35. M. Dohmen, M. Menzel, H. Wiese, J. Reckfort, F. Hanke, U. Pietrzyk, K. Zilles, K. Amunts, and M. Axer, "Understanding fiber mixture by simulation in 3D Polarized Light Imaging," *NeuroImage* **111**, 464–475 (2015).
36. J. Mollink, M. Kleinnijenhuis, A. V. C. Van Walsum, M. Jenkinson, M. Pallegage-gamarallage, O. Ansorge, S. Jbabdi, and K. L. Miller, "Evaluating fibre orientation dispersion in white matter: Comparison of diffusion MRI, histology and polarized light imaging," *NeuroImage* **157**, 561–574 (2017).
37. M. Menzel, M. Axer, H. De Raedt, I. Costantini, L. Silvestri, F. S. Pavone, K. Amunts, and K. Michielsen, "Toward a High-Resolution Reconstruction of 3D Nerve Fiber Architectures and Crossings in the Brain Using Light Scattering Measurements and Finite-Difference Time-Domain Simulations," *Phys. Rev. X* **10**(2), 021002 (2020).
38. S. Chang, J. Yang, A. Novoseltseva, X. Fu, C. Li, S. Chen, J. C. Augustinack, C. Magnain, B. Fischl, A. C. Mckee, D. A. Boas, I. A. Chen, and H. Wang, "Multi-Scale Label-free Human Brain Imaging with Integrated Serial Sectioning Polarization Sensitive Optical Coherence Tomography and Two-Photon Microscopy," (2023).

39. W. S. Tiffany Lam and R. Chipman, "Balancing polarization aberrations in crossed fold mirrors," *Appl. Opt.* **54**(11), 3236 (2015).
40. H. Wang, C. Magnain, S. Sakadžić, B. Fischl, and D. A. Boas, "Characterizing the optical properties of human brain tissue with high numerical aperture optical coherence tomography," *Biomed. Opt. Express* **8**(12), 5617 (2017).
41. J. Yang, I. A. Chen, S. Chang, J. Tang, B. Lee, K. Kılıç, S. Sunil, H. Wang, D. Varadarajan, C. Magnain, S.-C. Chen, I. Costantini, F. Pavone, B. Fischl, and D. A. Boas, "Improving the characterization of ex vivo human brain optical properties using high numerical aperture optical coherence tomography by spatially constraining the confocal parameters," *Neurophotonics* **7**(04), 1–16 (2020).
42. C. J. Liu, W. Ammon, R. J. Jones, J. Nolan, R. Wang, S. Chang, M. P. Frosch, A. Yendiki, D. A. Boas, C. Magnain, B. Fischl, and H. Wang, "Refractive-index matching enhanced polarization sensitive optical coherence tomography quantification in human brain tissue," *Biomed. Opt. Express* **13**(1), 358 (2022).
43. M. Menzel, J. Reckfort, D. Weigand, H. Köse, K. Amunts, and M. Axer, "Diatenuation of Brain Tissue and its Impact on 3D Polarized Light Imaging," *Biomed. Opt. Express* **8**(7), 3163 (2017).
44. P. Berens, "CircStat: A MATLAB Toolbox for Circular Statistics," *J. Stat. Soft.* **31**(10), 1–21 (2009).
45. S. Chang, D. Varadarajan, J. Yang, I. A. Chen, S. Kura, C. Magnain, J. C. Augustinack, B. Fischl, D. N. Greve, D. A. Boas, and H. Wang, "Scalable mapping of myelin and neuron density in the human brain with micrometer resolution," *Sci. Rep.* **12**(1), 363 (2022).
46. M. Menzel, J. A. Reuter, D. Gräfel, I. Costantini, K. Amunts, and M. Axer, "Automated computation of nerve fibre inclinations from 3D polarised light imaging measurements of brain tissue," *Sci. Rep.* **12**(1), 4328 (2022).
47. R. Turner, "Myelin and modeling: Bootstrapping cortical microcircuits," *Front. Neural Circuits* **13**, 1–11 (2019).
48. I. S. Buyanova, M. Arsalidou, and R. Turner, "Cerebral White Matter Myelination and Relations to Age, Gender, and Cognition: A Selective Review," *Front. Hum. Neurosci.* **15**, 1–22 (2021).
49. O. Sporns and R. F. Betzel, "Modular brain networks," *Annu. Rev. Psychol.* **67**(1), 613–640 (2016).
50. M. D. Budde and J. A. Frank, "Examining brain microstructure using structure tensor analysis of histological sections," *NeuroImage* **63**(1), 1–10 (2012).
51. I. Ronen, M. Budde, E. Ercan, J. Annese, A. Techawiboonwong, and A. Webb, "Microstructural organization of axons in the human corpus callosum quantified by diffusion-weighted magnetic resonance spectroscopy of N-acetylaspartate and post-mortem histology," *Brain Struct. Funct.* **219**(5), 1773–1785 (2014).
52. A. R. Khan, A. Cornea, L. A. Leigland, S. G. Kohama, S. Nørhøj, and C. D. Kroenke, "3D structure tensor analysis of light microscopy data for validating diffusion MRI," *NeuroImage* **111**, 192–203 (2015).
53. K. G. Schilling, V. Janve, Y. Gao, I. Stepniewska, B. A. Landman, and A. W. Anderson, "Histological validation of diffusion MRI fiber orientation distributions and dispersion," *NeuroImage* **165**, 200–221 (2018).
54. C. Leuze, M. Goubran, M. Barakovic, M. Aswendt, Q. Tian, B. Hsueh, A. Crow, E. M. M. Weber, G. K. Steinberg, M. Zeineh, E. D. Plowey, A. Daducci, G. Innocenti, J. Thiran, K. Deisseroth, J. A. McNab, S. Processing, É Polytechnique, and F. De Lausanne, "Comparison of diffusion MRI and CLARITY fiber orientation estimates in both gray and white matter regions of human and primate brain," *NeuroImage* **228**, 117692 (2021).
55. A. J. Schain, R. A. Hill, and J. Grutzendler, "Label-free in vivo imaging of myelinated axons in health and disease with spectral confocal reflectance microscopy," *Nat. Med.* **20**(4), 443–449 (2014).
56. Y. Fu, H. Wang, T. B. Huff, R. Shi, and J.-X. Cheng, "Coherent anti-Stokes Raman scattering imaging of myelin degradation reveals a calcium-dependent pathway in lyso-PtdCho-induced demyelination," *J. Neurosci. Res.* **85**(13), 2870–2881 (2007).
57. P. Gasecka, A. Jaouen, F. Z. Bioud, H. B. de Aguiar, J. Duboisset, P. Ferrand, H. Rigneault, N. K. Balla, F. Debarbieux, and S. Brasselet, "Lipid Order Degradation in Autoimmune Demyelination Probed by Polarized Coherent Raman Microscopy," *Biophys. J.* **113**(7), 1520–1530 (2017).
58. A. Ozsvár, R. Szpócs, Z. Ozsvár, J. Baka, P. Barzó, G. Tamás, and G. Molnár, "Quantitative analysis of lipid debris accumulation caused by cuprizone induced myelin degradation in different CNS areas," *Brain Res. Bull.* **137**, 277–284 (2018).
59. I. Costantini, E. Baria, M. Sorelli, F. Matuschke, F. Giardini, M. Menzel, G. Mazzamuto, L. Silvestri, R. Cicchi, K. Amunts, M. Axer, and F. S. Pavone, "Autofluorescence enhancement for label-free imaging of myelinated fibers in mammalian brains," *Sci. Rep.* **11**(1), 8038 (2021).
60. M. Sorelli, I. Costantini, L. Bocchi, M. Axer, F. S. Pavone, and G. Mazzamuto, "Fiber enhancement and 3D orientation analysis in label-free two-photon fluorescence microscopy," *Sci. Rep.* **13**(1), 4160 (2023).
61. M. A. Wallenburg, M. F. G. Wood, N. Ghosh, and I. A. Vitkin, "Polarimetry-based method to extract metrics of tissue anisotropy," *Opt. Lett.* **35**(15), 2570–2572 (2010).
62. C. J. Liu, A. J. Black, H. Wang, and T. Akkin, "Quantifying three-dimensional optic axis using polarization-sensitive optical coherence tomography coherence tomography," *J. Biomed. Opt.* **21**(7), 070501 (2016).
63. N. Ugryumova, S. V. Gangnus, and S. J. Matcher, "Three-dimensional optic axis determination using variable-incidence-angle polarization-optical coherence tomography," *Opt. Lett.* **31**(15), 2305–2307 (2006).
64. N. Ugryumova, J. Jacobs, M. Bonesi, and S. J. Matcher, "Novel optical imaging technique to determine the 3-D orientation of collagen fibers in cartilage: variable-incidence angle polarization-sensitive optical coherence tomography," *Osteoarthr. Cartil.* **17**(1), 33–42 (2009).
65. Y. Wang, M. Ravanfar, K. Zhang, D. Duan, and G. Yao, "Mapping 3D fiber orientation in tissue using dual-angle optical polarization tractography," *Biomed. Opt. Express* **7**(10), 3855 (2016).

66. M. Axer and K. Amunts, "Scale matters: The nested human connectome," *Science* **378**(6619), 500–504 (2022).
67. M. Menzel, M. Ritzkowski, J. A. Reuter, D. Gräbel, K. Amunts, and M. Axer, "Scatterometry Measurements With Scattered Light Imaging Enable New Insights Into the Nerve Fiber Architecture of the Brain," *Front. Neuroanat.* **15**, 767223 (2021).
68. M. Menzel, J. A. Reuter, D. Gräbel, M. Huwer, P. Schlömer, K. Amunts, and M. Axer, "Scattered Light Imaging: Resolving the substructure of nerve fiber crossings in whole brain sections with micrometer resolution," *NeuroImage* **233**, 117952 (2021).